Computation of Axisymmetric Suction Flow Through Porous Media in the Presence of Surface Tension

Hector D. Ceniceros

Department of Mathematics, University of California Santa Barbara, Santa Barbara, California 93106

and

Helen Si

Oracle Corporation, 500 Oracle Parkway, Redwood Shores California 94065

E-mail: hdc@math.ucsb.edu; hsi@us.oracle.com

The effect of small surface tension on a class of axi-symmetric flows with suction is studied numerically. The dynamic evolution of a blob of incompressible viscous fluid, surrounded by air, and drawn into an interior sink is considered. The velocity field of the viscous fluid is assumed to satisfy Darcy's law and thus, the motion is that of a flow through porous media. The fluid interface motion is computed using a highly accurate boundary integral method. This method combines recent numerical techniques to achieve efficient and high order space and time discretizations for this type of flows. Through accurate computations, it is shown that, in the presence of small surface tension, the dynamic behavior of the axi-symmetric flows is very similar to that of the (two-dimensional) Hele-Shaw counterparts. A long finger develops in the fluid interface and forms a cone singularity when it reaches the sink before all the fluid is sucked out. The finger bulges and develops a neck for sufficiently small surface tension. The bulge-neck formation is enhanced by the additional component of the mean curvature in the three-dimensional flow. However, its effect is not strong enough to cause the interface to pinch-off at the neck for the data considered here.

Key Words: Hele-Shaw flow, boundary integral method, singularity formation

1. INTRODUCTION

Suction driven flows through porous media are of considerable interest to the oil industry. In a recovery process, oil surrounded by water is extracted through a well (sink) via a suction mechanism. Often, this type of flows are modeled by the two-dimensional (2-D) motion of a viscous fluid through a narrow gap between two parallel plates in a device known as a Hele-Shaw cell. The connection of these so-called Hele-Shaw flows with saturated flows through porous media is Darcy's law which is assumed to govern the motion of both flows. Darcy's law states that the velocity field is proportional to the gradient of the pressure. The particular case of a Hele-Shaw flow in which a blob of viscous fluid such as oil, surrounded by less viscous fluid, is driven through a sink has attracted considerable attention. Laboratory experiments [16] have shown that the surrounding fluid encroaches upon the oil forming long "fingers" which may reach the sink before all the oil is recovered.

Recently [7], Ceniceros, Hou, and Si investigated numerically the effects of small surface tension in the fingering process that occurs in a Hele-Shaw flow with suction. They found that an asymptotic finger shape is selected in the limit as surface tension goes to zero. The fluid interface collapses forming a corner at the tip of the finger when it reaches the sink. It was also found in [7] that, for sufficiently small surface tension, the encroaching finger develops a neck which also appears to asymptote to corners in the limit as surface tension tends to zero. But there were no indications that the Hele-Shaw interface would pinch off at the finger neck creating a topological singularity in the form of a bubble of the less viscous fluid. The initial data considered in [7] was a circular interface offset from a point sink. Since surface tension acts on the fluid interface by introducing a jump in the pressure proportional to the mean curvature, it is natural to ask what the behavior of the interface would be in a three-dimensional (3-D) Darcy flow for similar initial conditions. Can topological singularities occur in 3-D for this particular type of flow? How does the presence of an additional component of the mean curvature affect the fingering process? Here, we investigate numerically these questions. We consider the 3-D axi-symmetric Darcy (potential) flow consisting of a blob of incompressible viscous fluid surrounded by air and driven through a point sink located inside the blob.

The accurate computation of the axi-symmetric flows described above is full of numerical difficulties; especially in the presence of surface tension. Boundary integral methods are a popular choice to compute accurately a certain class of free boundary problems which includes potential flows. These methods reduce the dimension of the problem by involving only variables on the fluid interface. However, this reduction is done at the expense of introducing singular boundary integrals which are understood in the sense of principal-value integrals. In 2-D motion, the boundary integrals can be desingularized and spectrally accurate approximations may be obtained for closed or periodic interfaces in the horizontal direction [17, 18]. In 3-D motion, the boundary integrals are much more difficult to treat. In the case of axi-symmetric flow, the integrands contain a complex combination of pole and logarithmic singularities. Even if the leading order singularities are extracted, some derivative of the integrands will be singular and, as a result, standard quadrature rules will have a non-smooth discretization error. Moreover, as noted by Baker, Meiron, and Orszag [3], the integrands change rapidly at the two poles where the surface intersects the axis of symmetry. This makes the accurate evaluation of the principal-value integrals even more difficult to achieve. It is important to note that a non-smooth error, i.e., with many high frequency components whose amplitudes do not decay and are well above machine precision, can quickly lead to numerical instability and cause the computations to break down.

For the axi-symmetric flow, de Bernadinis and Moore [5] proposed a quadrature rule for the boundary integrals with a correction to the vortex ring method to obtain an $O(h^3 \log h)$ approximation. In the vortex ring method the trapezoidal rule is used omitting the self-induced (diagonal) contribution of each vortex ring. However, de Bernadinis and Moore approximation (dBM) gives a non-smooth error which degenerates to $O(h)$ near the symmetry poles. Nitsche [15] has designed a clever improvement to the dBM quadrature by constructing approximate integrands near the poles. By integrating the difference between the original and the approximate integrands, Nitsche obtained a uniform $O(h^3)$ quadrature. Nitsche has also shown that higher order quadratures are possible by improving the order of the approximate integrands [14]. Nie and Baker [12] have also proposed accurate quadratures for the evaluation of the boundary integrals in axi-symmetric flow. Their approximations are based on adaptive local quadratures near the poles. Here, we use Nitsche's fifth order quadrature [14]. The high order quadrature is needed for both accuracy and stability reasons. To maintain numerical stability the non-smooth components of the discretization error must be removed, through numerical filtering, after each evaluation of the boundary integrals. Unfortunately, for one of the cases we study, the fluid interface deformes the most precisely at one of the symmetry poles. As a result, the accuracy of the quadrature, which is based on a Taylor expansion around the poles, deteriorates. If the lower order $O(h^3)$ quadrature is used, the non-smooth error becomes so large that it cannot be controled by numerical filtering and, consequently, it leads to numerical instability and to a quick breakdown of the computations.

Surface tension introduces additional difficulties to the computation of the dynamically evolving fluid interface. It modifies the pressure on the interface by a term which is proportional to the local mean curvature. As a result, a nonlinear term with high order derivatives is introduced to the interface governing equations through the mean curvature. This surface tension term induces a severe time step stability constraint for explicit time marching methods. Hou, Lowengrub, and Shelley [9] have designed a technique to successfully remove the severe stability constraint. The technique is based on a small-scale decomposition of the governing equations and on the application of implicit/explicit time integration schemes. Here, we use the method of Hou, Lowengrub, and Shelley implemented with a fourth order implicit/explicit multi-step scheme.

Our numerical results show that the axi-symmetric flow with suction in the presence of small surface tension behaves very similarly to the corresponding Hele-Shaw flow. The first case we study is an initially spherical blob of incompressible viscous fluid surrounded by air. The blob is drawn into an eccentric point sink inside it. Just as in the Hele-Shaw flows, a narrow finger develops. The finger tip evolves into a cone and appears to develop a curvature singularity when the interface reaches the sink. For sufficiently small surface tension, the finger bulges and a well defined neck forms at the top of the finger. The additional azimuthal component of the mean curvature enhances the definition of the finger neck while smoothing the interface there at the same time. However, this component of the curvature is not large enough to induce the neck to pinch off. The second case we consider is the evolution of a slightly perturbed spherical interface whose associated Hele-Shaw problem was studied numerically by Nie and Tian [13]. As in the Hele-Shaw flow, two long fingers grow close to the axis of symmetry and also appear to develop cones at their tips as they reach the sink. For both initial data, we observe that the axi-symmetric flow develops narrower fingers than those found in the Hele-Shaw counterpart. This may be due to the stronger sink force in the 3-D flow.

The organization of the rest of the paper is as follows. In Section 2, we present the equations of motion for the axi-symmetric flow through porous media in a boundary integral formulation. We describe the numerical method in Section 3. The main idea to construct the uniform order quadratures of Nitsche is outlined here. We also explain how to adapt the technique of Hou, Lowengrub, and Shelley to obtain an efficient non-stiff time discretization for the computation of the axi-symmetric flow in the presence of surface tension. Several important numerical issues such as numerical stability and filtering are also discussed in Section 3. As a test to the numerical method, we compute the evolution of an initially spherical vortex sheet [12, 14]. Section 4 is devoted to present the numerical results on the axi-symmetric flow with suction along with some comparisons with the corresponding Hele-Shaw flow. Concluding remarks are given in Section 5.

2. THE GOVERNING EQUATIONS

We consider an axi-symmetric blob of incompressible viscous fluid surrounded by air or gas whose density is so light (compared to that of the viscous fluid) that the motion of the gas is unimportant. The velocity field $\mathbf{u}$ of the viscous fluid is given by Darcy's law:

$$\mathbf{u} = -\frac{k}{\mu}\nabla p, \tag{1}$$

where k is the permeability of the medium, μ is the viscosity of the fluid, and p is the pressure. The incompressibility of the fluid expressed as $\nabla \cdot \mathbf{u} = 0$ implies that the pressure satisfies Laplace's equation

$$\nabla^2 p = 0. \tag{2}$$

The nonlinearity of the flow comes from the boundary conditions on the fluid interface (the boundary of the fluid blob). Denoting the interface by Γ, these conditions can be written in the following form:

$$\begin{aligned} [\mathbf{u}\cdot\hat{\mathbf{n}}]|_\Gamma &= 0, & (3)\\ [p]|_\Gamma &= \tau\kappa, & (4) \end{aligned}$$

where $[\cdot]$ denotes the jump across the interface. Here, $\hat{\mathbf{n}}$ is the exterior unit normal to Γ, τ is the surface tension coefficient, and κ is the mean curvature of the interface. The kinematic boundary condition (3) states that the normal component of the velocity field is continuous across the interface. This implies that particles on the interface remain there. The relation (4), known as the Laplace-Young boundary condition, gives an account of how the presence of surface tension modifies the pressure across the interface. As explained in [4], for an actual porous medium, the quantities in (4) have the meaning of a statistical average taken over the void space (pore) in the vicinity of the point considered. Thus, in general, the surface

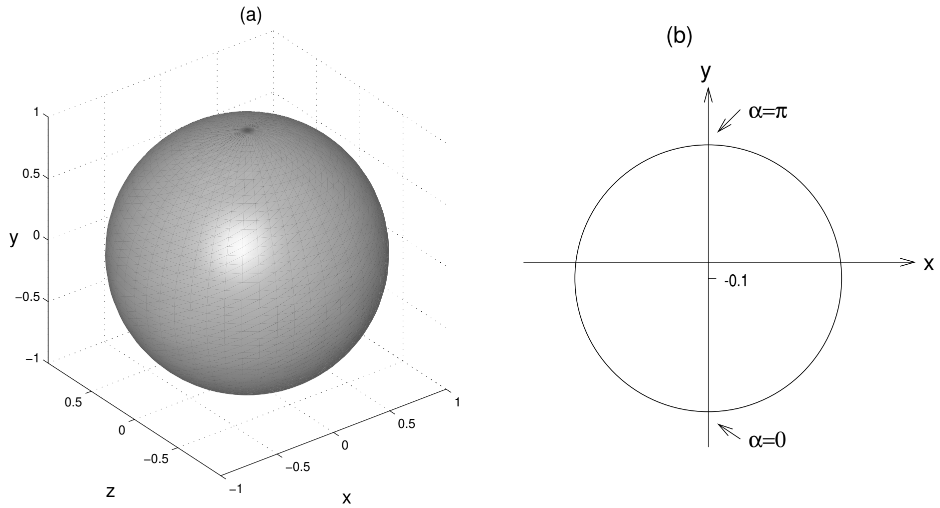

FIG. 1. Spherical surface: (a) 3-D perspective and (b) curve representing the cross section of the flow in the $x-y$ plane.

tension coefficient τ depends locally on the geometry of each pore, on the degree of saturation, and of the type of fluids involved. Here we restrict ourself with the idealized case when τ is constant.

We assume that there is a point sink at the origin, inside the fluid blob. For large distances away from the sink, the velocity field tends to the simple 3-D radial flow:

$$\mathbf{u}(\mathbf{X}) \to Q_s \frac{\mathbf{X}}{|\mathbf{X}|^3}, \quad \text{as } |\mathbf{X}| \to \infty, \tag{5}$$

where Q_s is the sink strength or suction rate (assumed negative). Since the flow is potential, it can be described by the dynamics of the free interface Γ. Furthermore, we assume that the flow is axi-symmetric. Thus, the surface Γ can be represented by its cross section with the x-y plane, as depicted in Fig. 1 for the case of a spherical surface. At any time t, we write Γ in parametric form as $(x(\alpha,t), y(\alpha,t))$, where α is a Lagrangian parameter. Both x and y are 2π periodic functions in α. Note that, because of symmetry, $(x(\alpha,t), y(\alpha,t))$ with $\alpha \in [0,\pi]$ suffices to describe the whole interface.

Taking into account the sink, the radial (u) and axial (v) velocities are given by [6]

$$\begin{aligned} u(\alpha,t) &= \frac{1}{2\pi x}\int_0^\pi \gamma' \frac{y'-y}{\rho_2}\left[F(\lambda) - \frac{(y'-y)^2 + x'^2 + x^2}{\rho_1^2} E(\lambda)\right] d\alpha' \\ &\quad + Q_s \frac{x}{(x^2+y^2)^{3/2}}, \end{aligned} \tag{6}$$

$$\begin{aligned} v(\alpha,t) &= \frac{1}{2\pi}\int_0^\pi \gamma' \frac{1}{\rho_2}\left[F(\lambda) - \frac{(y'-y)^2 + x'^2 - x^2}{\rho_1^2} E(\lambda)\right] d\alpha' \\ &\quad + Q_s \frac{y}{(x^2+y^2)^{3/2}}, \end{aligned} \tag{7}$$

where $\rho_1^2 = (y-y')^2 + (x-x')^2$ and $\rho_2^2 = (y-y')^2 + (x+x')^2$. Here γ is the analogue to the 2-D unnormalized vortex sheet strength, i.e., it is the jump in the tangential velocity times $\sqrt{x_\alpha^2 + y_\alpha^2}$. $F(\lambda)$ and $E(\lambda)$ are the complete elliptic integrals of the first and second kind given by:

$$\begin{aligned} F(\lambda) &= \int_0^{\frac{\pi}{2}} \frac{d\theta}{\sqrt{1-\lambda^2\cos^2\theta}}, \\ E(\lambda) &= \int_0^{\frac{\pi}{2}} \sqrt{1-\lambda^2\cos^2\theta}\, d\theta, \end{aligned}$$

with $\lambda^2 = 4xx'/\rho_2^2$. The integrals in (6) and (7) are understood as principal-value integrals. Following the derivation for Hele-Shaw flow (see, for example [7, 19]), we get a similar integral equation for γ at the cross section with the x-y plane:

$$\gamma(\alpha, t) = \frac{2}{s_\alpha}(x_\alpha u + y_\alpha v) + S\kappa_\alpha. \tag{8}$$

Here, $S = \tau k/\mu$, is a scaled surface tension parameter. Thus, the motion of the axi-symmetric flow through porous media with suction is described by (6), (7), and (8). We nondimensionalize the equations of motion by setting $Q_s = -1$ and by taking the initial radius of the interface to be 1. Finally, the mean curvature can be computed using the following formula:

$$\kappa = \frac{x_\alpha y_{\alpha\alpha} - x_{\alpha\alpha} y_\alpha}{s_\alpha^3} + \frac{y_\alpha}{x s_\alpha}, \tag{9}$$

where $s_\alpha = \sqrt{x_\alpha^2 + y_\alpha^2}$. For future reference, we write the two components of the curvature separately as

$$\begin{aligned} \kappa_1 &= \frac{x_\alpha y_{\alpha\alpha} - x_{\alpha\alpha} y_\alpha}{s_\alpha^3}, && (10) \\ \kappa_2 &= \frac{y_\alpha}{x s_\alpha}. && (11) \end{aligned}$$

We see that the governing equations are very similar to those for the 2-D Hele-Shaw flow, except for the additional component κ_2 of the mean curvature, and the integrands of the boundary integrals. Also, the point sink has a different form.

3. THE NUMERICAL METHOD

There are two main components in obtaining a numerical solution to the initial value problem given by (6), (7), and (8): an accurate discretization in space which includes the evaluation of the principal-value integrals and the solution of the integral equation for γ, and an efficient and accurate time marching scheme. The appropriate choice of each discretization is nontrivial as the boundary-integral formulation is very sensitive to numerical instabilities. In addition, in the presence of small surface tension, discretetizations become even more sensitive due to the ill-posedness of the underlying zero-surface-tension problem [8, 10]. We describe in this section our discretization choices and illustrate why high accuracy and delicate numerical filtering are required to compute reliably the nonlinear interface evolution.

3.1. Evaluation of the principle-value integrals

Unlike the case for the analogous 2-D motion, the integrands in the boundary integrals for 3-D axi-symmetric flow have a very complex structure involving poles and logarithmic singularities. Even if the leading order singularities are extracted, some derivative of the integrands will be singular and as a result standard quadrature rules will have a non-smooth discretization error. Moreover, as noted by Baker, Meiron, and Orszag [3], the integrands change rapidly at the two poles where the surface intersects the axis of symmetry. This makes the accurate evaluation of the principal-value integrals for axi-symmetric flow even more difficult to achieve.

Here, we use a high order quadrature due to Nitsche [15]. This quadrature originally developed to achieve a uniform $O(h^3)$ discretization error has been extended by Nitsche [14] to yield an $O(h^5)$ error. This fifth order quadrature is used for the all computations accounted here. We present next only the main ideas in the construction of Nitsche's quadrature. The presentation is based on the description of the quadrature given in [15, 14]. We refer the reader to these references for the details.

Each boundary integral can be written in the following form:

$$w(\alpha, t) = \int_0^\pi G(\alpha, \alpha', t) d\alpha', \tag{12}$$

where

$$G(\alpha, \alpha', t) = G(\gamma(\alpha', t), x(\alpha, t), y(\alpha, t), x(\alpha', t), y(\alpha', t)) \tag{13}$$

is a function given in terms of the elliptic integrals $F(\lambda)$ and $E(\lambda)$ as expressed in Eq. (6) and Eq. (7). Note that there is a different G for each boundary integral. Expanding the elliptic integrals around $\lambda = 1$ and performing a Taylor expansion around $\alpha' = \alpha$, it follows that

$$G(\alpha, \alpha', t) = G_s(\alpha, \alpha', t) + \frac{c_{-1}(\alpha, t)}{\alpha' - \alpha} + \sum_{k=0}^{\infty} c_k(\alpha, t)(\alpha' - \alpha)^k \log|\alpha' - \alpha|, \tag{14}$$

where $G_s(\alpha, \alpha', t)$ is a smooth function in both α and α'. Consider a uniform mesh in α given by $\alpha_i = ih$ for $i = 0, 1, \ldots, N$ and $h = \pi/N$. Sidi and Israeli [18] show that

$$\begin{aligned}\int_0^\pi G(\alpha_i, \alpha', t) d\alpha' \;=\; & h \sum_{j \neq i} G(\alpha_i, \alpha_j, t) + hG_s(\alpha_i, \alpha_j, t) + c_0(\alpha_i, t) h \log \frac{h}{2\pi} \\ & + \sum_{k=2}^{2m} \nu_k c_k(\alpha_i, t) h^{k+1} \\ & + \sum_{k=1}^{2m+1} \gamma_k [\frac{\partial^k}{\partial \alpha'^k} G(\alpha_i, \pi, t) - \frac{\partial^k}{\partial \alpha'^k} G(\alpha_i, 0, t)] h^{k+1} \\ & + O(h^{2m+3}) \end{aligned} \tag{15}$$

for any integer $m \geq 1$. The constants ν_k and γ_k (not to be confused with the vortex sheet strength γ) are given in [18]. The first term in the right-hand side of (15) corresponds to the ring vortex approximation while the first three terms together give the de Bernadinis and Moore quadrature. Quadratures of higher order may be constructed by approximating the principal-value integral by the right-hand side of (15) for a given $m \geq 1$. However, the error for all these quadratures is nonuniform and deteriorates severely near the poles of the symmetry axis ($\alpha = 0$ and $\alpha = \pi$). As pointed out by Nitsche [15], this is because both the coefficients c_k and the derivatives $\partial^k G / \partial {\alpha'}^k$ are not uniformly bounded. In fact, Nitsche [15] shows that, as $\alpha_i \to 0$, they behave asymptotically as

$$c_k(\alpha_i, t) \sim \frac{1}{\alpha_i^{k-1}} \qquad \text{and} \qquad \frac{\partial^k}{\partial {\alpha'}^k} G(\alpha_i, 0, t) \sim \frac{1}{\alpha_i^{k-1}}, \tag{16}$$

for the boundary integral in the radial velocity u given by (6), and as

$$c_k(\alpha_i, t) \sim \frac{1}{\alpha_i^{k}} \qquad \text{and} \qquad \frac{\partial^k}{\partial {\alpha'}^k} G(\alpha_i, 0, t) \sim \frac{1}{\alpha_i^{k}}, \tag{17}$$

for the boundary integral in the axial velocity v given by (7). Similar estimates hold for $\alpha_i \to \pi$.

The main idea of Nitsche's quadrature is to construct functions B^0 and B^π that approximate G at the symmetry poles to get corrections for the nonuniform quadratures derived from (15). The functions B^0 and B^π are obtained by Taylor expanding the integrand G about the poles $\alpha = 0$ and $\alpha = \pi$. Let us denote any of the nonuniform quadrature rules by $Q[\cdot]$. Near $\alpha = 0$, $G - B^0$ is smoother than G and consequently $Q[G - B^0] = Q[G] - Q[B^0]$ has a smoother discretization error than $Q[G]$. Therefore, the approximation

$$\int_0^\pi G d\alpha' \approx Q[G] - Q[B^0] + \int B^0 d\alpha' \tag{18}$$

behaves better than $Q[G]$ near $\alpha = 0$. Note that

$$E_Q[B^0] = \int B^0 d\alpha' - Q[B^0] \tag{19}$$

acts as a local correction to the error in $Q[G]$. A similar correction $E_Q[B^\pi]$ can be obtained near $\alpha = \pi$. The final approximation due to Nitsche [15] can be written as

$$\int_0^\pi G(\alpha_i, \alpha', t) d\alpha' \approx Q[G] + w_1(\alpha_i) E_Q[B^0] + w_2(\alpha_i) E_Q[B^\pi], \tag{20}$$

where w_1 and w_2 are positive weight functions that satisfy $w_1 + w_2 = 1$. Both $E_Q[B^0]$ and $E_Q[B^\pi]$ can be computed efficiently with a very small overhead to $Q[G]$. Except for simple factors, the corrections are time-independent and can be precomputed. As noted by Nitsche [14], due to cancellation of digits, the time-indepentdent terms in the corrections need to be precomputed using quadruple precision to achieve the $O(h^5)$ quadrature. This quadrature is obtained from (15) for $m = 1$ and the appropriate corrections $E_Q[B^0]$ and $E_Q[B^\pi]$.

3.2. Time integration: removing the surface-tension induced stiffness

Through the curvature, surface tension introduces high order derivatives of the interface position that couple nonlinearly and nonlocally with the flow. The presence of high order space derivatives causes a severe time step stability constraint for explicit time integration schemes. Hou, Lowengrub, and Shelley [9] have designed an ingenious technique to remove the severe stability constraint usually referred to as stiffness. Their technique is based on the fact that the stiffness arises only at the small scales of the numerical solution. Thus, the crux of the method of Hou, Lowengrub, and Shelley is to perform a small-scale decomposition of the equations of motion and to treat implicitly the leading order terms at small scales. Here, we adapt this technique to the axi-symmetric flow equations. The implicit discretization is simplified by expressing the position of the interface cross section curve (x, y) in terms of the local tangent angle $\theta = \tan^{-1}(y_\alpha/x_\alpha)$ and the arc-length metric $s_\alpha = \sqrt{x_\alpha^2 + y_\alpha^2}$. In these two new variables, the 2-D component of the mean curvature becomes $\kappa_1 = \theta_\alpha/s_\alpha$ and the interface evolution equations are given by

$$s_{\alpha t} = T_\alpha - \theta_\alpha U, \tag{21}$$

$$\theta_t = \frac{1}{s_\alpha}(U_\alpha + T\theta_\alpha), \tag{22}$$

where T and U are the interface tangential and normal velocity respectively. The stiffness is hidden at the small spatial scales of U_α in the θ-equation (22). The leading order behavior of U at small scales can be obtained by noting that, for $x \neq 0$, the leading order terms of the integrands in the velocity [Eq. (6) and Eq. (7)] are

$$-\frac{2x\gamma y_\alpha}{s_\alpha^2(\alpha' - \alpha)} \quad \text{and} \quad \frac{2\gamma x_\alpha}{s_\alpha^2(\alpha' - \alpha)} \tag{23}$$

for the radial and axial velocity respectively. Therefore, it can be easily shown that

$$U(\alpha, t) \sim \frac{1}{2s_\alpha}\mathcal{H}[\gamma](\alpha, t), \tag{24}$$

where $\mathcal{H}$ is the Hilbert transform which is diagonalizable by the Fourier transform as $\hat{\mathcal{H}}[f] = -i\text{sign}(k)\hat{f}$. The notation $f \sim g$ means that the difference between f and g is smoother than f and g. Moreover, γ is dominated by the surface tension term $S\kappa_1$ at small scales, that is

$$\gamma(\alpha, t) \sim S\kappa_{1\alpha} = S\left(\frac{\theta_\alpha}{s_\alpha}\right)_\alpha. \tag{25}$$

Therefore,

$$U(\alpha, t) \sim \frac{S}{2s_\alpha}\mathcal{H}[(\theta_\alpha/s_\alpha)_\alpha](\alpha, t). \tag{26}$$

This dominant term at small scales simplifies if the arc-length metric s_α is constant in space. This can be achieved by exploiting the freedom in selecting the tangential velocity, as the interface motion is solely determined by the normal velocity U. By letting

$$T(\alpha,t)=\int_0^{\alpha}\theta_{\alpha'}U d\alpha'-\frac{\alpha}{2\pi}\int_0^{2\pi}\theta_{\alpha'}U d\alpha', \tag{27}$$

s_α is maintained constant and equal to its mean at all times, i.e., $s_\alpha = L(t)/2\pi$, where $L(t)$ is the total length of the curve in the cross section at time t. The equations of motion can now be written as

$$L_t = -\int_0^{2\pi}\theta_{\alpha'}U d\alpha', \tag{28}$$

$$\theta_t = \frac{S}{2}\left(\frac{2\pi}{L}\right)^3 \mathcal{H}[\theta]_{\alpha\alpha\alpha}+P, \tag{29}$$

where P represents lower order terms at small spatial scales. L can be updated by an explicit method as Eq. (28) is free of stiffness. To remove the high-order stiffness, it is sufficient to discretize implicitly the leading order term in Eq. (29) and to treat the lower order term P explicitly. This gives a linear time step stability constraint, i.e., $\Delta t \leq Ch$, where Δt is the time step size and C is a constant. Moreover, because of its constant coefficients, the implicit term can be easily inverted by using the fast Fourier transform (FFT). Here, we use the following fourth order explicit/implicit method studied by Ascher, Ruuth, and Wetton [1]

$$\begin{aligned}&\frac{1}{\Delta t}\left(\frac{25}{12}\theta^{n+1}-4\theta^{n}+3\theta^{n-1}-\frac{4}{3}\theta^{n-2}+\frac{1}{4}\theta^{n-3}\right)=\\ &\frac{S}{2}\left(\frac{2\pi}{L^{n+1}}\right)^3\mathcal{H}[\theta^{n+1}]_{\alpha\alpha\alpha}+4P^n-6P^{n-1}+4P^{n-2}-P^{n-3}.\end{aligned} \tag{30}$$

L is updated first using a fourth order explicit Adams-Bashforth multi-step scheme to obtain L^{n+1} before computing θ^{n+1} via FFT. The spatial derivatives are computed also using FFT.

Note that, at each time step, γ has to be obtained from the integral Eq. (8) to compute the velocities. As pointed out by Baker, Meiron, and Orszag [2], (8) can be solved efficiently by fixed point iteration accelerated with a good initial guess. Here, we use a fourth order extrapolated initial guess constructed from previous time steps. It typically takes a few iterations to obtain a convergent solution for γ when the interface is relatively smooth.

3.3. Filtering and numerical stability

To test our implementation of the fifth order quadrature for the evaluation of the principal-value boundary integrals, we compute the motion of a vortex sheet in a homogeneous incompressible inviscid fluid in the absence of surface tension. This test example allows us also to illustrate some important issues concerning numerical stability. We use the following initial data:

$$x(\alpha,0)=\cos(\alpha), \qquad y(\alpha,0)=\sin(\alpha), \qquad \gamma(\alpha,0)=\cos(\alpha),$$

which corresponds to the cross section of a spherical sheet. This is the problem computed by Nitsche [15], and by Nie and Baker [12], using two different quadratures. Note that for this problem, γ is constant in time and only the interface

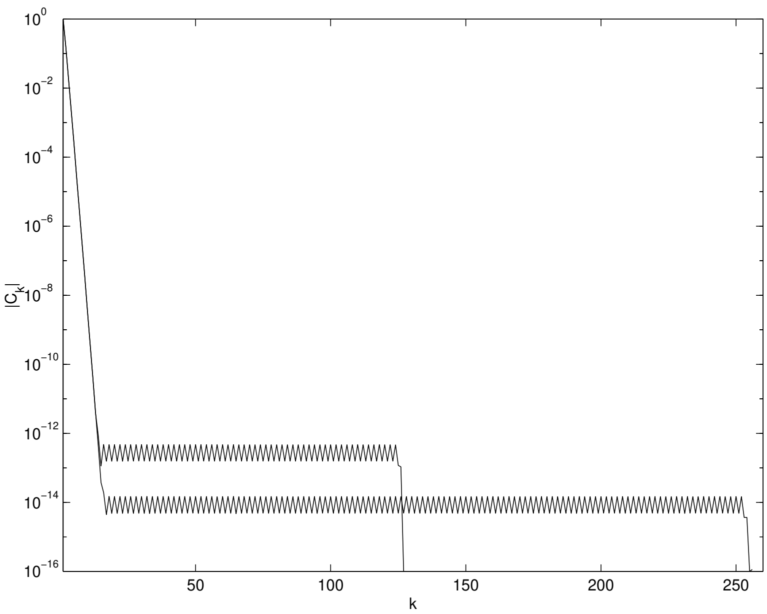

FIG. 2. Fourier spectrum of the velocity $u + iv$ for the initial data of the spherical vortex sheet. The velocity was computed using the fifth order quadrature with $N = 256$ and $N = 512$.

position needs to be updated. Thus, the computational cost is significantly less than that of the axi-symmetric suction flow where γ has to be obtained from the integral Eq. (8) every time step.

Figure 2 shows the Fourier spectrum of the boundary integrals for the initial data. This is a plot of the magnitude of the Fourier coefficients of the complex vortex sheet velocity $u + iv$ [Eq. (6) and Eq. (7) with $Q_s = 0$]. The integrals are computed using Nitsche's fifth order quadrature with $N = 256$ and $N = 512$. Here N is the total number of uniformly spaced points along the complete interface ($\alpha \in [0, 2\pi]$). Note that there is a plateau of high frequency modes for each N. The plateau comes from the non-smooth discretization error. Its level decreases by approximately a factor of 32 when the resolution is doubled. If this plateau is not removed, the coupling of the interface position with the velocity will cause a rapid growth of the numerical solution high frequency modes, and this will in turn lead to numerical instability.

Krasny filtering [11] provides a way of removing the high frequency modes introduced by the non-smooth discretization error in the velocity integrals. Given a grid-defined function f_i, Krasny filter is implemented by taking the FFT of f_i, setting to zero all the Fourier modes of f_i whose magnitude are below a certain level, and transforming back. Note that to maintain accuracy, the filter level must be chosen as low as possible. Typically, it is selected in the order of 10^3 times the round-off error.

Using the $L - \theta$ formulation given by (28) and (29) with $N = 2048$ points and $\Delta t = 0.0001$, we compute the motion of the initially spherical vortex sheet. At every time step, the velocity is filtered with a level set to 7.5×10^{-11}. All the computations presented here are performed with standard double precision. In addition, to prevent the spurious growth of round-off error high-frequency modes under the Kelvin-Helmholtz instability, Krasny filtering is applied to θ with a filter level set to 10^{-13}. Figure 3 shows the interface profile, the mean curvature, and the spectrum of the velocity at $t = 1.09$. Figure 3(b) gives clear indications of a curvature singularity developing at the interface. The spectrum of the velocity is free of any sign of numerical instability.

It is important to note that the vortex sheet remains smooth at the poles $\alpha = 0$ and $\alpha = \pi$ at all times. As we will see in the next section, this is not the case for the axi-symmetric flows we are interested in. Since the quadrature we use is based on a Taylor expansion about the symmetry poles, the accuracy deteriorates as the poles lose regularity. Very high spatial resolution is required to maintain the high frequency components of the non-smooth discretization error below an acceptable filter level. In addition, γ couples with the principal-value boundary integrals through the integral equation (8). This extra coupling makes the computation more sensitive to numerical instability than that for a vortex sheet where γ is constant (zero surface tension) or explicitly determined (with surface tension). In our implementation, the integral equation (8) is solved iteratively. The iteration process is stopped when the difference between two subsequent iterations is less than a tolerance set to 10^{-11}. Krasny filtering is applied to u and v given by (6) and (7) in every iteration used to solve for γ. The filter level for u and v is selected lower (smaller) than 10^{-11} to guarantee the convergence of the iterations up to the tolerance level but high enough so that the non-smooth part of the error is removed. After the iterations are completed at every time step, γ is also filtered with a filter level slightly higher than the iteration tolerance. To summarize, filtering is applied as follows for the computation of the axi-symmetric flow interface motion:

- Filter θ every time step with a level set to 10^{-13}. This is a typical filter level for double precision computations.
- Filter u and v for every iteration used to solve for γ with a level equal to 10^{-12}.
- Filter γ after the iterations are completed at every time step with a level set to 2.5×10^{-11}.
- Filter the boundary integrals (u and v) with a level set to 7.5×10^{-11} to compute the normal velocity. This filter level is higher because of the filtering applied to γ.

4. NUMERICAL RESULTS

We now present the numerical results obtained for two different sets of initial data: a spherical interface centered at $(0, -0.1, 0)$ (see Fig. 1) and a slightly perturbed spherical interface corresponding to one of the Hele-Shaw flows considered by Nie and Tian [13]. In both cases the sink is located at the origin. Most of the computations start with $N = 512$ and $\Delta t = 0.0001$. N is doubled before all the Fourier modes of the tangent angle $\theta(\alpha, t)$ are above the filter level equal to 10^{-13}. The time step Δt is selected so that decreasing it further would not produce any appreciable difference within plotting resolution in the curvature of the interface. At the same time, Δt is chosen sufficiently small so that with Krasny filtering applied every time step, the growth of the high frequency components introduced by the discretization error in the boundary integrals is kept under control. This is in effect what dictates the size of Δt and not the surface tension stiffness which has

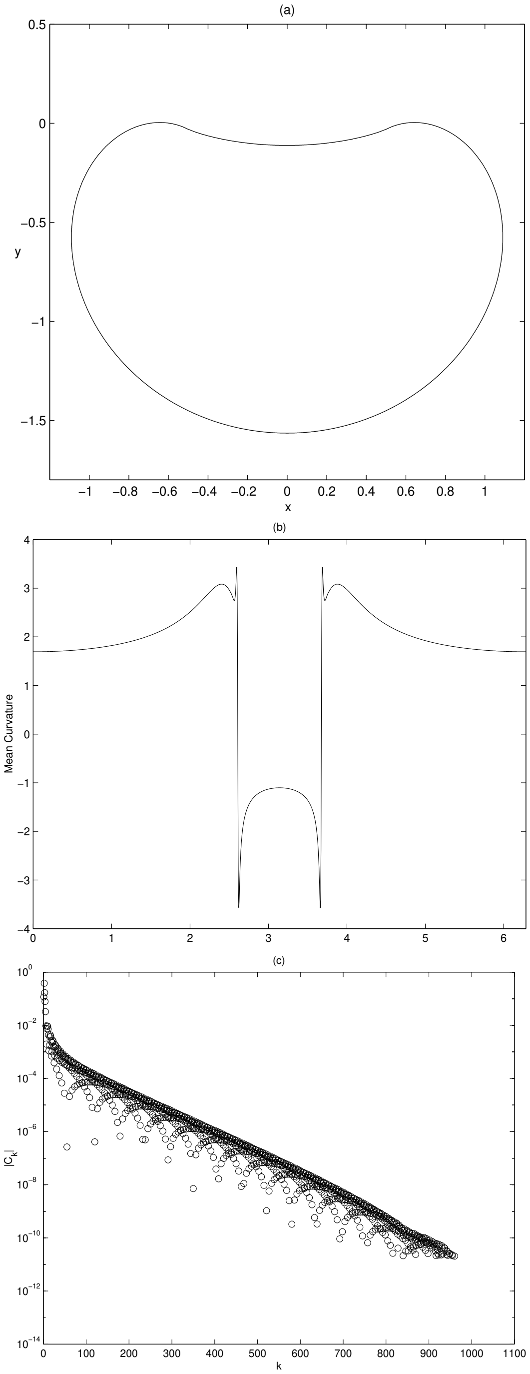

FIG. 3. Vortex sheet test run. These plots correspond to $t = 1.09$ with $N = 2048$ and $\Delta t = 0.0001$. (a) Cross section of the vortex sheet. (b) Mean curvature versus α. (c) Fourier coefficient $|c_k|$ of the complex velocity $u + iv$.

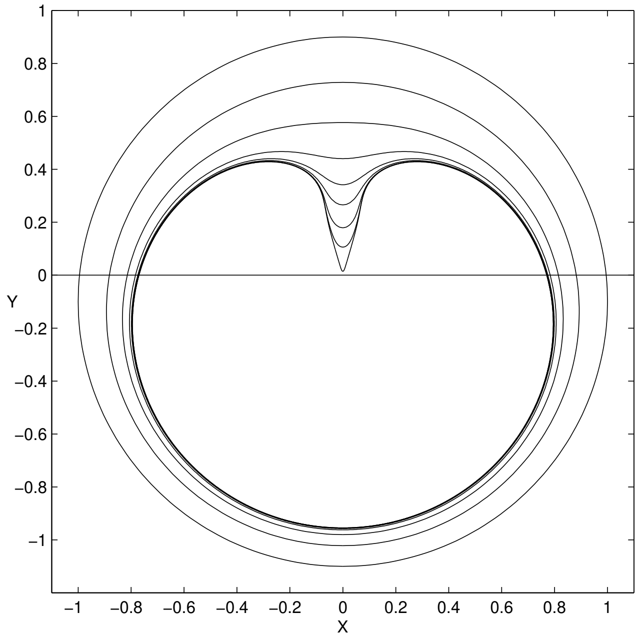

FIG. 4. Evolution of the initially spherical blob of fluid with $S = 0.01$. The interface profiles, from the outer perimeter inwards, correspond to the times $t = 0$, 0.1, 0.15, 0.171, 0.1768, 0.1786, 0.1795, 0.1798, and 0.179876. $N = 4096$ and $\Delta t = 5 \times 10^{-8}$ for the last stage of the motion.

been removed by the technique of Hou, Lowengrub, and Shelley [9]. Indeed, we find that, before the interface begins to deform at one pole, the method we use has only the linear constraint $\Delta t \leq Ch$.

We consider first the initially spherical interface. Figure 4 shows the interface cross section profile at different times for $S = 0.01$. A 3-D perspective of the interface for the last computed time $t = 0.179876$ is presented in Fig. 5. Just as in the Hele-Shaw flow, a thin finger develops. As it gets closer to the sink, the finger evolves rapidly into a cone. The cone forms much earlier than the wedge in the Hele-Shaw flow. Also, the diameter of the top of the finger is smaller for the axi-symmetric flow. These differences may be due in part to the stronger suction force in the 3-D flow. We stop the computation when the distance of the cone tip to the sink is 0.0148. At this time, the formation of a corner singularity at the tip of the cone as it reaches the sink is evident. This can be clearly appreciated in the plot of the tangent angle $\theta(\alpha, t)$ in Fig. 6. The angle appears to develop a discontinuity at the finger tip ($\alpha = \pi$). The mean curvature at the tip at that time is around -671. We use $N = 4096$ and $\Delta t = 5 \times 10^{-8}$ for the last stage of the computation. This is the maximum resolution we can afford and, as we explain next, it is also the minimum resolution needed to compute the motion up to this stage.

As mentioned before, the accuracy in the evaluation of the boundary integrals in the equations of motion relies on the smoothness of the interface at the symmetry poles $\alpha = 0$ and $\alpha = \pi$. However, for the initial data we just considered, the interface is the least smooth, and eventually singular, precisely at one of the poles where the finger develops. As a result, we are forced to increase the spatial

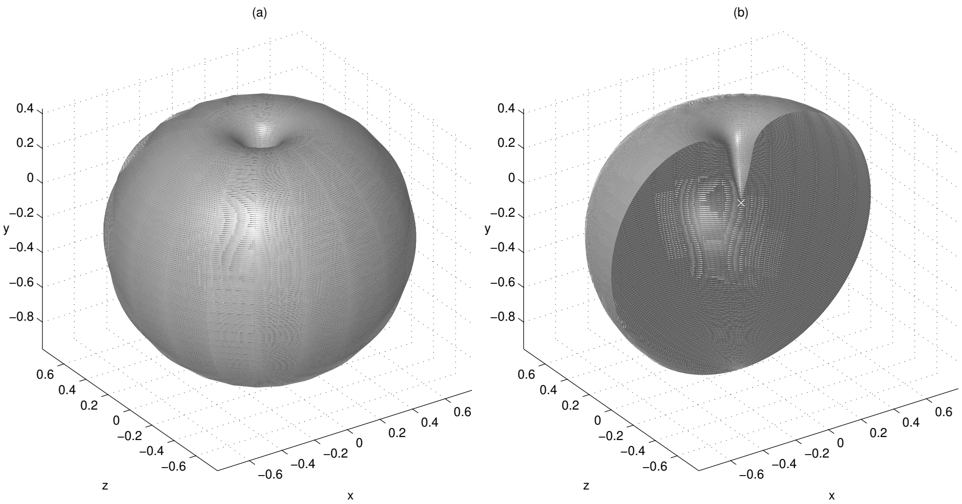

FIG. 5. The fluid surface for $S = 0.01$ at $t = 0.179876$. (a) 3-D perspective. (b) Cut-away plot. The cross marks the position of the sink.

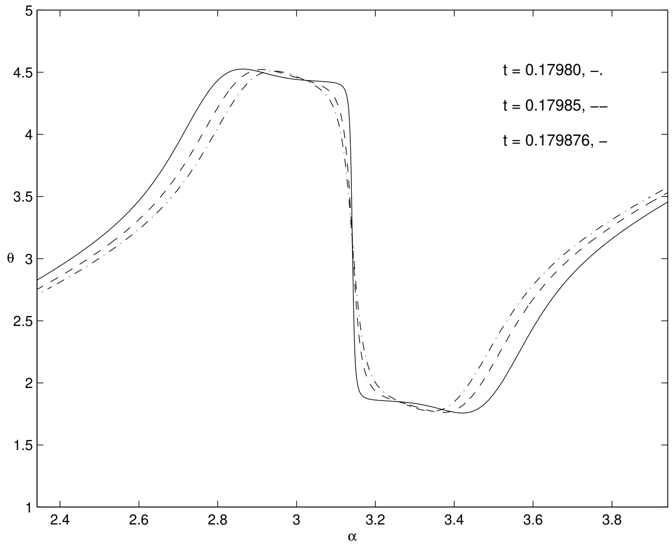

FIG. 6. Behavior of the tangent angle $\theta(\alpha, t)$ around the finger tip ($\alpha = 0$) as the interface is about to collapse, for $S = 0.01$. The tangent angle, plotted against α at the times $t = 0.17980$, $t = 0.17985$, and $t = 0.179876$, appears to develop a discontinuity. $N = 4096$ and $\Delta t = 1 \times 10^{-7}$ for $t = 0.17980$ and $t = 0.17985$. $N = 4096$ and $\Delta t = 5 \times 10^{-8}$ for $t = 0.179876$.

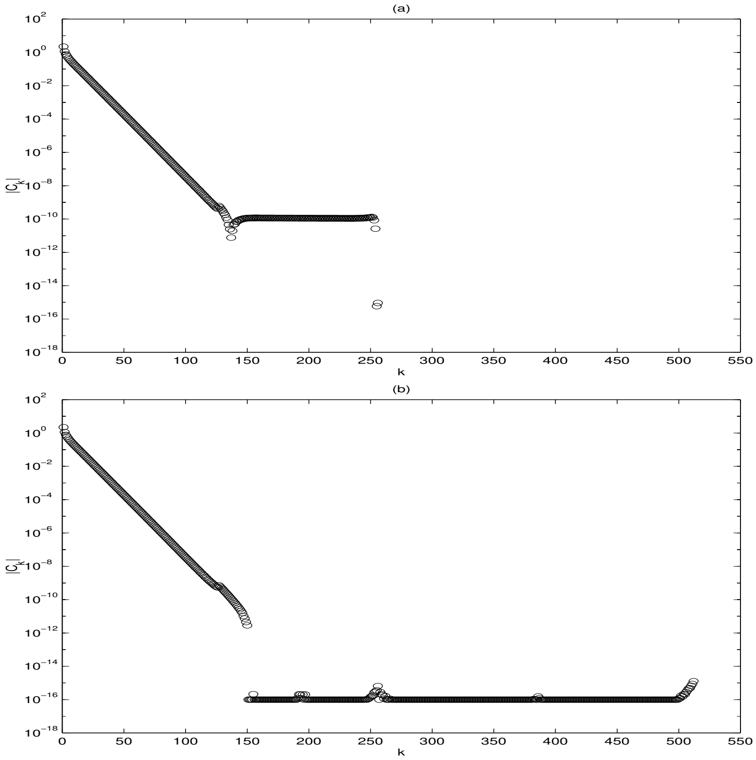

FIG. 7. The Fourier coefficients $|c_k|$ of the normal velocity at $t = 0.1723$: (a) $N = 512$ and (b) $N = 1024$.

resolution to maintain accuracy and to keep the non-smooth discretization error in the approximation of the boundary integrals below our filter level. Figure 7 shows the spectrum of the normal velocity for two different resolutions at $t = 0.1723$, right after the interface begins to deform at the north pole $\alpha = \pi$. As illustrated by this figure, it is necessary to use $N = 1024$ to have the plateau of high frequency components below the filter level. Note that this happens well before all the Fourier modes of the numerical solution have been used for the $N = 512$ resolution.

An additional factor that makes our computation very sensitive to numerical instability is the coupling of γ with the principal-value boundary integrals. This coupling occurs through the integral equation which is solved for γ iteratively every time step. After the iterations are completed at every time step, Krasny filtering is also applied to γ. The time step Δt is selected sufficiently small so that, with Krasny filtering applied to θ and γ every time step, the growth of the discretization error in the boundary integrals is kept under control. Figure 8 shows that a very small Δt is required to suppress the growth of unstable high frequency modes in the normal velocity.

We now decrease the surface tension to the value $S = 4 \times 10^{-4}$. Figure 9 shows the interface cross section profile at various times. The developed finger now clearly bulges and a well defined neck is observed. As remarked in the introduction, this interface behavior is reminiscent of what has been observed for the 2-D Hele-Shaw flow with suction [7]. In the Hele-Shaw flow the blob of fluid, just as in the axi-symmetric flow, obeys Darcy's law but it is confined to a 2-D motion by two closely

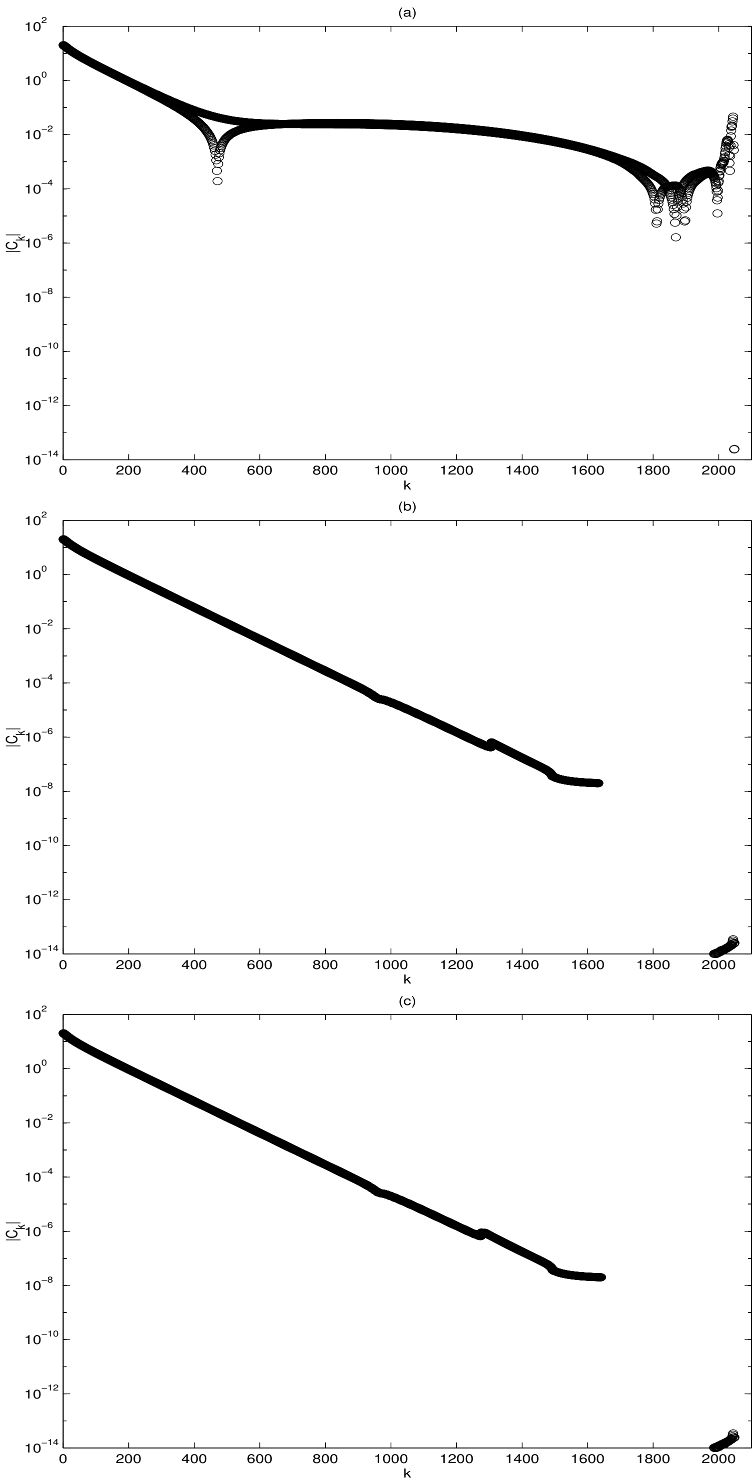

FIG. 8. The Fourier coefficients $|c_k|$ of the normal velocity at $t = 0.17987$ with $N = 4096$: (a) $\Delta t = 2 \times 10^{-7}$; (b) $\Delta t = 1 \times 10^{-7}$; (c) $\Delta t = 5 \times 10^{-8}$.

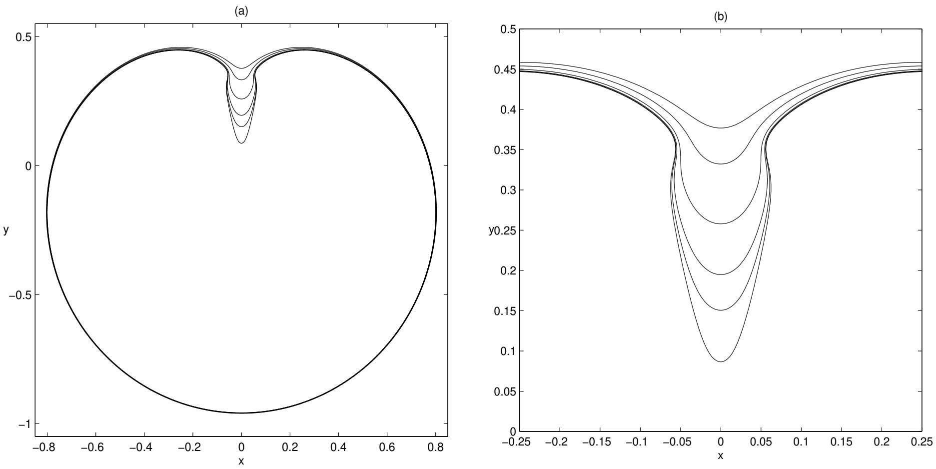

FIG. 9. Evolution of the fluid interface for $S = 4 \times 10^{-4}$. (a) The interface cross section profile plotted at $t = 0.1729$, 0.1739, 0.1749, 0.1754, 0.1756, and 0.175734. (b) A close-up of the finger formation. $N = 4096$ and $\Delta t = 2 \times 10^{-8}$ for the last stage of the motion.

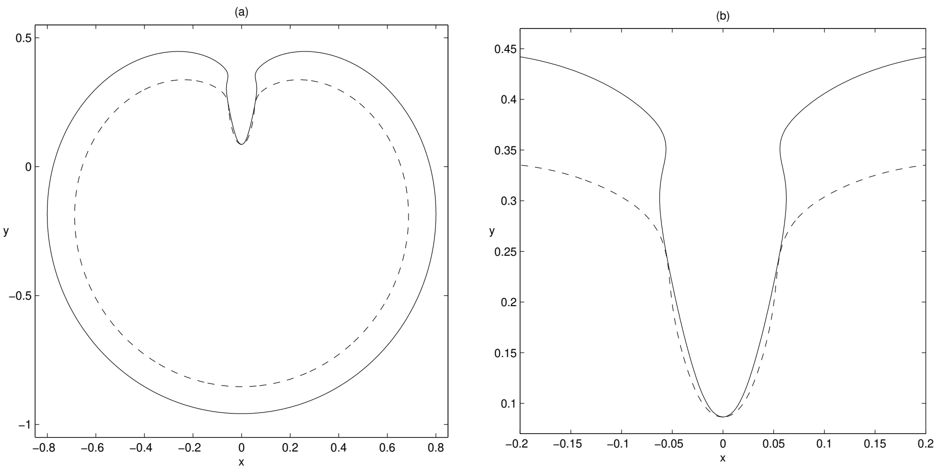

FIG. 10. (a) Cross section profile of the axi-symmetric flow at $t = 0.175734$ and the Hele-Shaw flow at $t = 0.2922625$ with the same surface tension $S = 4 \times 10^{-4}$. (b) A close-up look of the fingers. The solid curve corresponds to the axi-symmetric flow and the dashed line corresponds to the Hele-Shaw flow. $N = 4096$ and $\Delta t = 2 \times 10^{-8}$ for the axi-symmetric flow. $N = 2048$ and $\Delta t = 2.5 \times 10^{-6}$ for the Hele-Shaw flow.

spaced parallel plates. It is thus interesting to examine how the 3-D (axi-symmetric) flow compares with the 2-D (Hele-Shaw) counterpart. A comparison with the Hele-Shaw flow for the same value of surface tension appears in Fig. 10 (see [7] for the details of the Hele-Shaw study). The interfaces are not plotted at the same time t but when the tip of the finger reaches 0.0865 for both cases. The finger in the axi-symmetric flow shows a more visible bulging and a more pronounced neck. A curvature plot for these two interfaces given in Fig. 11 shows that the 2-D mean curvature κ_1 is more singular in the axi-symmetric flow. In Fig. 11, the two symmetric spikes correspond to the location of the neck while the two small dips next to the spikes correspond to the bulging area. The large negative spike at $\alpha = \pi$ points to the formation of a corner singularity.

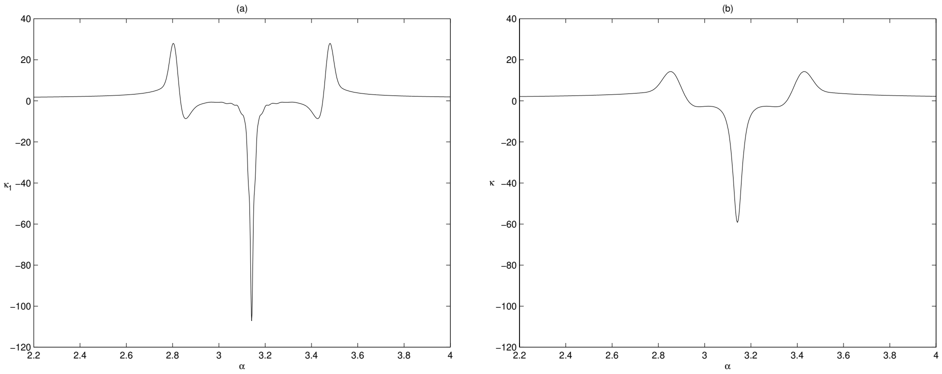

FIG. 11. Comparison of the interface 2-D mean curvature (κ_1) for the axi-symmetric and the Hele-Shaw flows with $S = 4 \times 10^{-4}$. (a) κ_1 versus α for the axi-symmetric flow at $t = 0.175734$. $N = 4096$ and $\Delta t = 2 \times 10^{-8}$. (b) κ_1 versus α for the Hele-Shaw flow at $t = 0.2922625$. $N = 2048$ and $\Delta t = 2.5 \times 10^{-6}$.

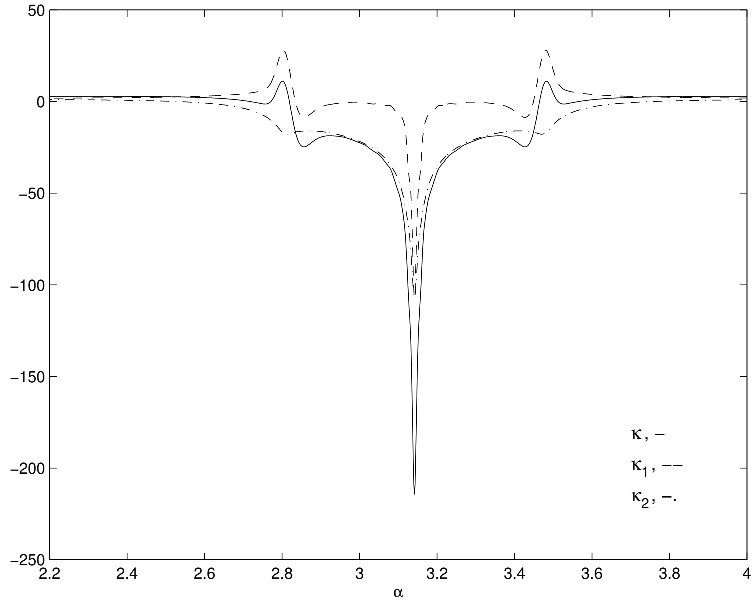

FIG. 12. Axi-Symmetric-flow curvature components at $t = 0.175734$ for $S = 4 \times 10^{-4}$. The solid line corresponds to $\kappa = \kappa_1 + \kappa_2$. The dashed line corresponds to κ_1 (2-D mean curvature) and the dashed-dotted line to κ_2. $N = 4096$ and $\Delta t = 2 \times 10^{-8}$.

In Fig. 12, we plot the two principal curvatures κ_1 and κ_2, and the mean curvature $\kappa = \kappa_1 + \kappa_2$ for the interface in the axi-symmetric flow with $S = 4 \times 10^{-4}$ at $t = 0.175734$. From this plot, we see the effect of the curvature in the axial direction. At the location of the neck, κ_1 has a positive spike while κ_2 is negative. This produces a reduced total mean curvature at the neck. But at the bulging area, immediately next to the neck, both κ_1 and κ_2 are negative and thus, together, enhance the finger bulging. For Hele-Shaw flow, there is an asymptotic shape of the fingers at the late stage of the interface motion [7]. We compare in Fig. 13 the interface profile for the axi-symmetric flow for $S = 4 \times 10^{-4}$ at $t = 0.175734$ and for $S = 8 \times 10^{-4}$ at $t = 0.176129$ when the finger tip reaches around 0.086. The finger

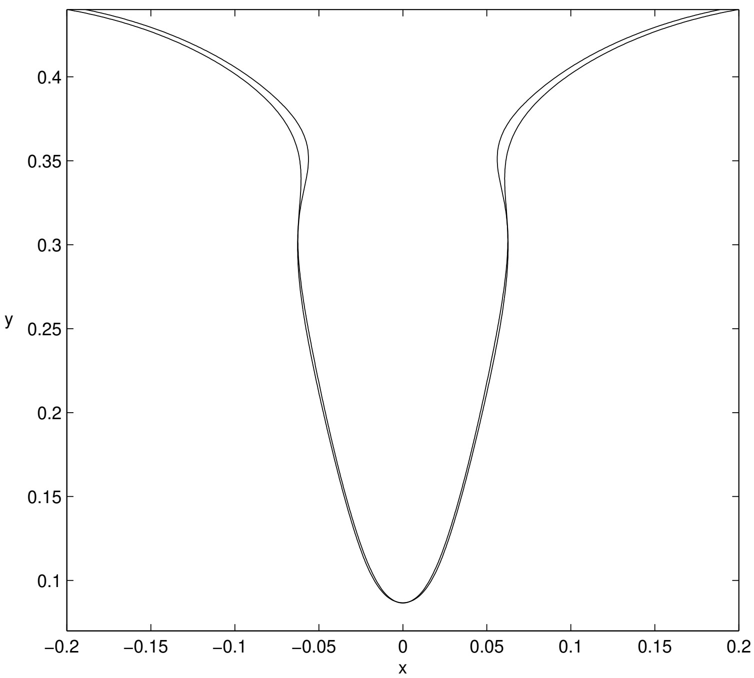

FIG. 13. Comparison of the interface finger in the axi-symmetric flow for two different values of surface tension, $S = 4 \times 10^{-4}$ at $t = 0.175734$ and $S = 8 \times 10^{-4}$ at $t = 0.176129$. $N = 4096$ and $\Delta t = 2 \times 10^{-8}$ for $S = 4 \times 10^{-4}$. $N = 4096$ and $\Delta t = 2.5 \times 10^{-8}$ for $S = 8 \times 10^{-4}$.

width varies very little away from the neck and an asymptotic shape is conceivable based on the similar behavior observed in the Hele-Shaw flow.

Next, we consider the second initial data which are generated by a particular exact solution of a Hele-Shaw flow with suction in the absence of surface tension. Unlike the 3-D axi-symmetric case, the Hele-Shaw flow may be described in terms of a conformal map from the interior (or exterior) of the unit disk onto the fluid blob. The circular boundary is mapped to the interface. Our second initial interface is produced by the conformal mapping [13]

$$f(\omega) = \alpha\omega + \frac{\beta\omega}{1 - \omega_0\omega}. \tag{31}$$

Here $f = x + iy$ and the coefficients α, β, and ω_0 are determined by the following system of equations (see [13] for details)

$$\begin{aligned} \alpha\beta + \alpha^2 &= r_1^2 + 1/2, &(32)\\ \frac{\beta^2}{(1-\omega_0^2)^2} + \alpha\beta &= r_2^2, &(33)\\ \frac{\omega_0}{1-\omega_0^2}\beta + \omega_0\alpha &= r_1 + r_2, &(34) \end{aligned}$$

with $r_1 = 0.7$ and $r_2 = 0.1$. After solving numerically (32), (33), and (34), we get $\alpha \approx 0.9902$, $\beta \approx 0.0094$, and $\omega_0 \approx 0.78799$. The mapping f generates a slightly perturbed circular profile in the x-y plane. The point sink is, as before, at the origin. This is one of the sets of initial data considered by Nie and Tian [13] for

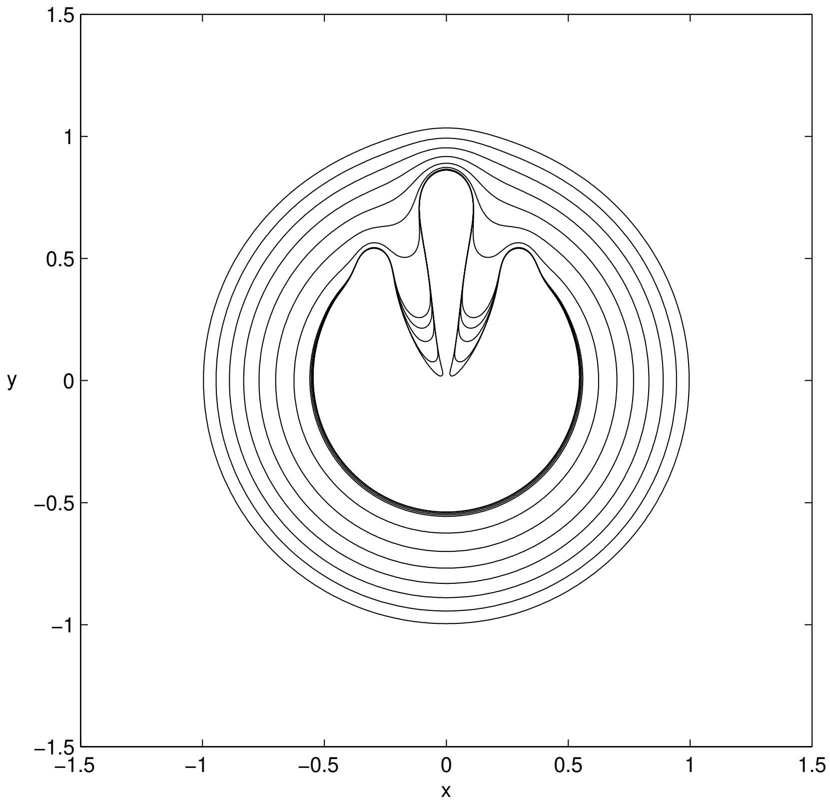

FIG. 14. Evolution of the "big and small circles" initial interface with $S = 0.002$ for a Hele-Shaw flow. The interface profiles, from the outer perimeter inwards, correspond to the times $t = k \times 0.05$ for $k = 0, \ldots, 6, t = 0.342 + k \times 0.04$, for $k = 0, \ldots, 4$, and $t = 0.355388$. $N = 4096$ and $\Delta t = 1 \times 10^{-6}$ for the last stage of the motion.

a Hele-Shaw flow with suction. In the absence of surface tension, the Hele-Shaw interface separates into one big and one small circle. Nie and Tian refer to this as the "big and small circle" data. One reason we choose this initial interface is that the fingers will not form at the poles and thus, the quadrature maintains its accuracy better.

Figure 14 presents the Hele-Shaw interface at various times with surface tension $S = 0.002$. Two long fingers form and approach the sink at the same pace. Each finger develops a corner at its tip when it touches the sink. In our computation for the axi-symmetric flow, we start with $N = 256$ points and we are able to use all the modes of the numerical solution before we double the number of points.

Figure 15 pictures the axi-symmetric flow interface at various times for $S = 0.002$. Similar to the Hele-Shaw flow, the interface forms two long fingers which are drawn into the sink. We stop our computation at $t = 0.283179$. At this stage we use $N = 4096$ and $\Delta t = 5 \times 10^{-7}$. Continuing the computation requires using $N = 8192$ points and turns out to be prohibitly expensive as the number of iterations to solve for γ also increases. The 3-D perspective of the fluid interface at $t = 0.283179$ is shown in Fig. 16. The sequence of pictures presented in Fig. 17 contrasts the differences between the Hele-Shaw and the axi-symmetric flow interfaces. Note that the central bulb is wider in the axi-symmetric flow but the fingers are thinner.

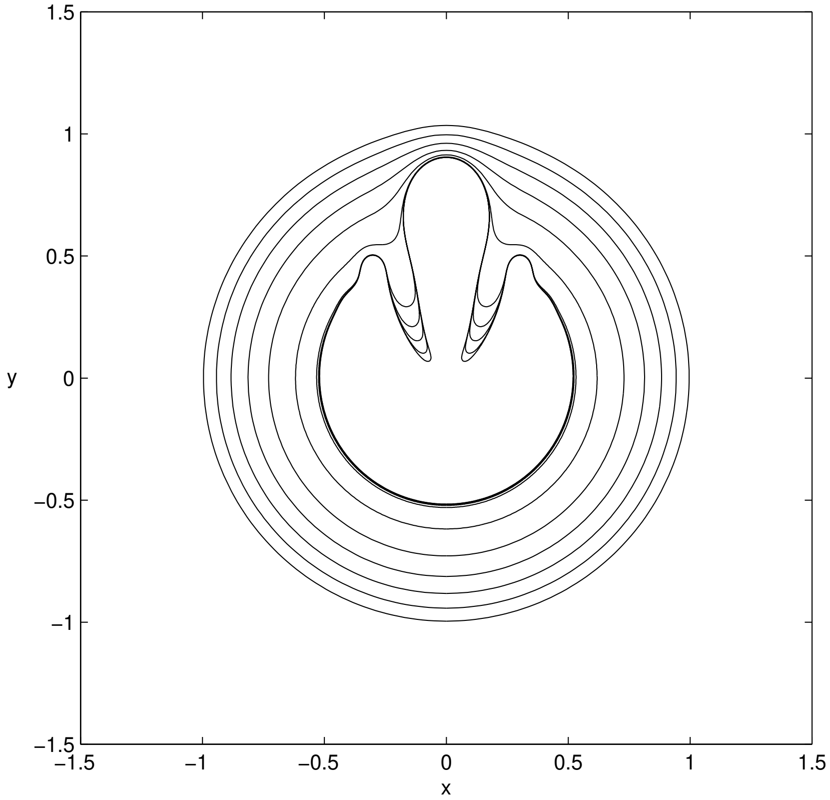

FIG. 15. Evolution of the fluid interface in the axi-symmetric flow for the slightly perturbed sphere corresponding to the 2-D "big and small circles" initial data with $S = 0.002$. The curves, from the outer perimeter inwards, correspond to the times $t = 0, 0.05$, 0.10, 0.15, 0.20, 0.25, 0.279, 0.2815, 0.2825, 0.283, and 0.283179. $N = 4096$ and $\Delta t = 5 \times 10^{-7}$ for the last stage of the motion.

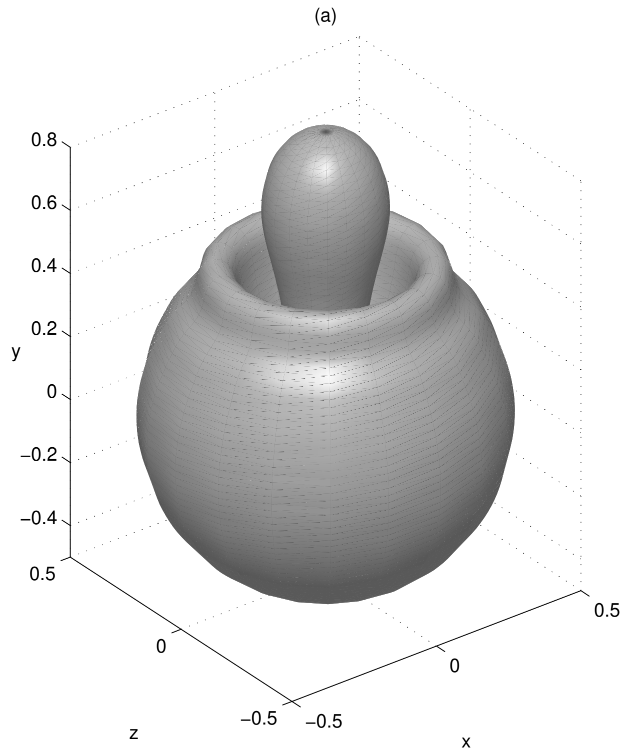

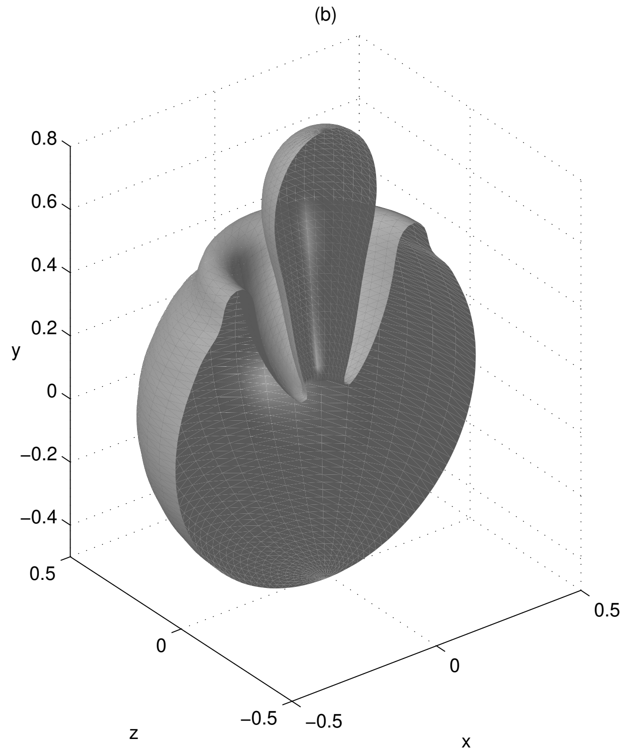

FIG. 16. The fluid interface for the slightly perturbed spherical initial surface ("big and small circle" data) for $S = 0.002$ at $t = 0.179876$. (a) 3-D perspective. (b) Cut-away plot.

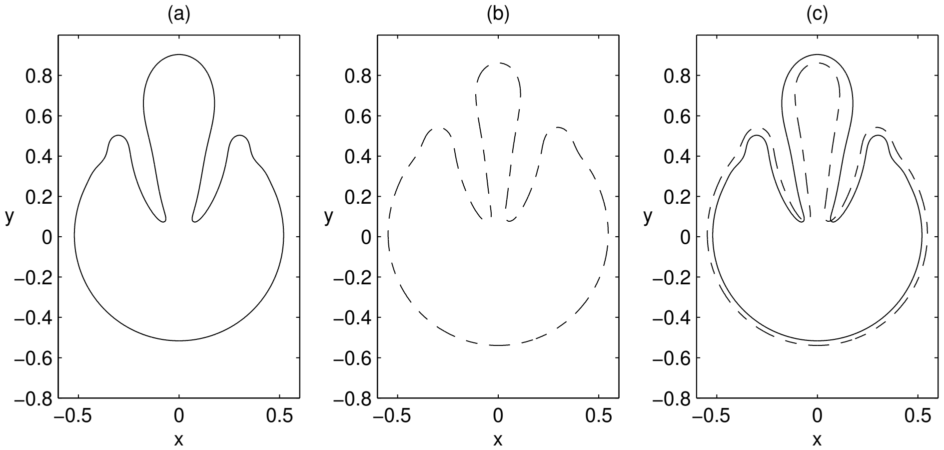

FIG. 17. Comparison of the axi-symmetric flow at $t = 0.283179$ with the Hele-Shaw flow at $t = 0.3542$. (a) Axi-Symmetric flow. (b) Hele-Shaw. (c) Both interfaces; solid line axi-symmetric flow and dashed line Hele-Shaw flow. $N = 4096$ and $\Delta t = 5 \times 10^{-7}$ for the axi-symmetric flow. $N = 2048$ and $\Delta t = 5 \times 10^{-6}$ for the Hele-Shaw flow.

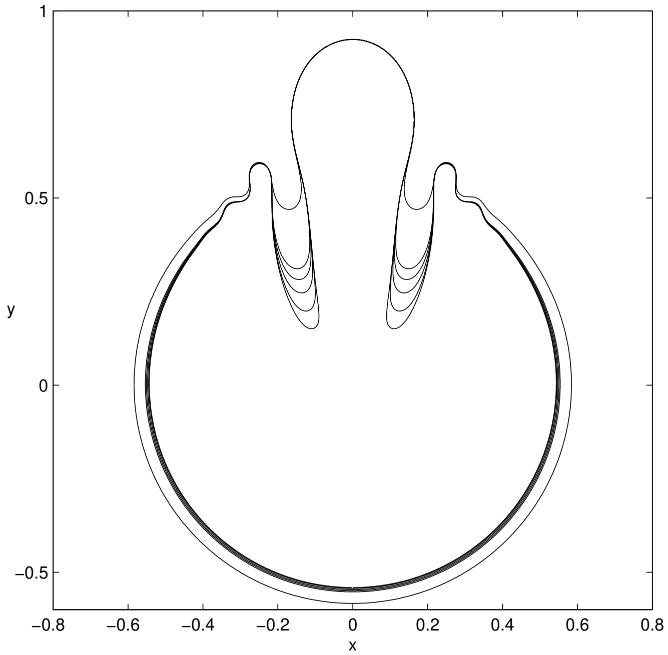

FIG. 18. Cross section interface profiles showing the evolution of the axi-symmetric flow for the slightly perturbed spherical initial data for $S = 5 \times 10^{-4}$ at $t = 0.2625$, 0.2725, 0.2735, 0.2745, 0.2755, and 0.276152. $N = 2048$ and $\Delta t = 2 \times 10^{-6}$ for the last stage of the computation.

We now decrease the surface tension to the value $S = 5 \times 10^{-4}$. Figure 18 shows the axi-symmetric flow interface at different times as it evolves. Due to the growth of the round-off error noise, and to the interface singular behavior, well resolved computations for such small values of surface tension are extremely difficult. We compare the profile of the interfaces for $S = 5 \times 10^{-4}$ and $S = 2.5 \times 10^{-4}$ in Fig. 19 when they reach around the same level in y. The oscillation next to the fingers is likely to be due to the influence of noise. Figure 19(b) shows the close-up plots of

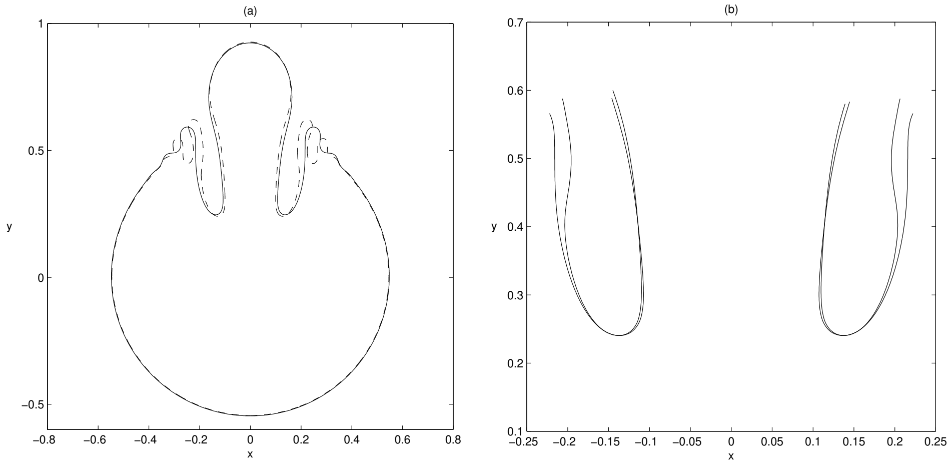

FIG. 19. Comparison of the interface profiles for the axi-symmetric flow with $S = 5 \times 10^{-4}$ at $t = 0.2745$ and $S = 2.5 \times 10^{-4}$ at $t = 0.275$. (a) Cross section profile. The solid line corresponds to $S = 5 \times 10^{-4}$ and the dashed line corresponds to $S = 2.5 \times 10^{-5}$. (b) Close-up look at the interface fingers. The inner curve is for $S = 2.5 \times 10^{-4}$, but it has been translated to align with the $S = 5 \times 10^{-4}$ fingers. $N = 2048$ and $\Delta t = 2 \times 10^{-6}$.

the two fingers. We shift the fingers for $S = 2.5 \times 10^{-4}$ in x direction to align with the $S = 5 \times 10^{-4}$ fingers to ease the comparison. For $S = 5 \times 10^{-4}$, the narrowest width for the finger is about 0.1, and it is about 0.06 for $S = 2.5 \times 10^{-4}$.

5. CONCLUSIONS

The accurate computation of axi-symmetric suction flow in the presence of surface tension requires a combination of numerical techniques to overcome the difficulties inherent to the problem. On one hand there is the numerical stiffness introduced by surface tension, on the other hand there is the lack of smoothness of the error produced by the quadrature rules for the (singular) principal-value integrals. While the surface-tension induced stiffness can be effectively removed by the application of the technique of Hou, Lowengrub, and Shelley [9], the non-smooth error coupled with the dynamic variables can quickly lead to strong numerical instability and to a computation breakdown. We have shown here that the combination of high accuracy both in space and time, and numerical filtering can be used to successfully suppress the unstable growth of the error.

Our series of computations demonstrate that the dynamic behavior of the axi-symmetric flow interface in the presence of small surface tension, is very similar to that of the corresponding (2-D) Hele-Shaw counterpart. The additional component of the mean curvature in the 3-D flow has a mild effect on the fingering process in the flows considered here and no topological singularity is observed. Of course, this does not exclude the possibility that a singularity of this type may form for different initial data or suction conditions.

ACKNOWLEDGMENT

We would like to thank Monika Nitsche who kindly provided us with all the details to implement her $O(h^5)$ method for evaluating the principal-value integrals. We would also like to thank Tom Hou for helpful suggestions and encouragement about this work.

REFERENCES

1. U. M. Ascher, S. J. Ruuth, and B. Wetton. Implicit-explicit methods for time-dependent pdes. *SIAM J. Numer. Anal.*, 32:797–823, 1995.
2. G. Baker, D. Meiron, and S. Orszag. Generalized vortex methods for free-surface flow problems. *J. Fluid Mech.*, 123:477–501, 1982.
3. G. R. Baker, D. I. Meiron, and S. A. Orszag. Boundary integral methods for axisymmetric and three-dimensional Rayleigh-Taylor instability problems. *Physica D*, 12:19–31, 1984.
4. J. Bear. *Dynamics of Fluids in Porous Media.* Dover Publications, Inc., New York, 1988.
5. B. De Bernadinis and D. W. Moore. *A ring-vortex representation of an axi-symmetric vortex sheet in Studies of Vortex Dominated Flows.* Springer, 1986.
6. R. E. Caflisch and X.-F. Li. Lagrangian theory for 3D vortex sheets with axial or helical symmetry. *Transport Theory Statist. Phys.*, 21:559, 1992.
7. H. D. Ceniceros, T.Y. Hou, and H. Si. Numerical study of Hele-Shaw flow with suction. *Physics of Fluids*, 11(9):2471–2486, 1999.
8. E. DiBenedetto and A. Friedman. The ill-posed Hele-Shaw model and the Stefan problem for supercooled water. *Trans. Am. Math. Soc.*, 282:183–204, 1984.
9. T.Y. Hou, J.S. Lowengrub, and M.J. Shelley. Removing the stiffness from interfacial flows with surface tension. *J. Comput. Phys.*, 114:312–338, 1994.
10. S.D. Howison, J.R. Ockendon, and A.A. Lacey. Singularity development in moving-boundary problems. *Q. J. Mech. Appl. Math.*, 38:343–360, 1985.
11. R. Krasny. A study of singularity formation in a vortex sheet by the point vortex approximation. *J. Fluid Mech.*, 167:65–93, 1986.
12. Q. Nie and G. Baker. Application of adaptive quadrature to axi-symmetric vortex sheet motion. *J. Comp. Phys.*, 143:49–69, 1998.
13. Q. Nie and F. R. Tian. Singularities in Hele-Shaw flows. *SIAM J. Appl. Math*, 58(1):34–54, 1998.
14. M. Nitsche. Singularity formation and roll-up of a cylindrical and spherical vortex sheet. Preprint,1999.
15. M. Nitsche. Axisymmetric vortex sheet motion: Accurate evaluation of the principal value integral. *SIAM J. Sci. Comput.*, 3:1066–1084, 1999.
16. L. Paterson. Radial fingering in a Hele-Shaw cell. *J. Fluid Mech.*, 113:513–529, 1981.
17. M. J. Shelley. A study of singularity formation in vortex sheet motion by a spectrally accurate vortex method. *J. Fluid Mech.*, 244:493–526, 1992.
18. A. Sidi and M. Israeli. Quadrature methods for periodic singular and weakly singular Fredholm integral equations. *J. Sci. Comp.*, 3:201–231, 1988.
19. G. Tryggvason and H. Aref. Numerical experiments in Hele-Shaw flows with a sharp interface. *J. Fluid Mech.*, 136:1–30, 1983.